Beam-on imaging of short-lived positron emitters during proton therapy

Buitenhuis, HJT; Diblen, F; Brzezinski, KW; Brandenburg, Sytze; Dendooven, P

Published in:
Physics in Medicine and Biology

DOI:
10.1088/1361-6560/aa6b8c

Publication date:
2017

Beam-on imaging of short-lived positron emitters during proton therapy

To cite this article before publication: Buitenhuis et al, 2017, Phys. Med. Biol., at press:
https://doi.org/10.1088/1361-6560/aa6b8c

Beam-on imaging of short-lived positron emitters during proton therapy

H J T Buitenhuis[1], F Diblen[1,*], K W Brzezinski[1], S Brandenburg[1] and P Dendooven[1]

[1] KVI-Center for Advanced Radiation Technology, University of Groningen, Zernikelaan 25, 9747 AA, Groningen, The Netherlands
[*] Currently at: Netherlands eScience Center, Science Park 140, 1098 XG Amsterdam, The Netherlands

E-mail: h.j.t.buitenhuis@rug.nl

Abstract

In-vivo dose delivery verification in proton therapy can be performed by positron emission tomography (PET) of the positron-emitting nuclei produced by the proton beam in the patient. A PET scanner installed in the treatment position of a proton therapy facility that takes data with the beam on will see very short-lived nuclides as well as longer-lived nuclides. The most important short-lived nuclide for proton therapy is ^{12}N (Dendooven *et al* 2015), which has a half-life of 11 ms. The results of a proof-of-principle experiment of beam-on PET imaging of short-lived ^{12}N nuclei are presented. The Philips Digital Photon Counting Module TEK PET system was used, which is based on LYSO scintillators mounted on digital SiPM photosensors. A 90 MeV proton beam from the cyclotron at KVI-CART was used to investigate the energy and time spectra of PET coincidences during beam on. Events coinciding with proton bunches, such as prompt gamma rays, were removed from the data via an anti-coincidence filter with the cyclotron RF. The resulting energy spectrum allowed good identification of the 511 keV PET counts during beam-on. A method was developed to subtract the long-lived background from the ^{12}N image by introducing a beam-off period into the cyclotron beam time structure. We measured 2D images and 1D profiles of the ^{12}N distribution. A range shift of 5 mm was measured as 6 ± 3 mm using the ^{12}N profile. A larger, more efficient, PET system with a higher data throughput capability will allow beam-on ^{12}N PET imaging of single spots in the distal layer of an irradiation with an increased signal-to-background ratio and thus better accuracy. A simulation shows that a large dual panel scanner, which images a single spot directly after it is delivered, can measure a 5 mm range shift with millimeter accuracy: 5.5 ± 1.1 mm for 1×10^8 protons and 5.2 ± 0.5 mm for 5×10^8 protons. This makes fast and accurate feedback on the dose delivery during treatment possible.

1 Introduction

Particle beam radiotherapy offers advantages over conventional photon radiotherapy. The Bragg peak dose profile has a finite depth and most of the dose is delivered at the end of the particle range. For specific tumor sites, these physical properties enable the creation of treatment plans that deliver less dose to co-irradiated normal tissue. This either allows dose escalation to the tumor at comparable dose-levels to normal tissue, or reduces the occurrence of radiation-induced side effects for the same level of tumor control. However, compared to photon radiotherapy, the delivered dose distribution is more sensitive to deviations from the situation on which the treatment plan is based. These deviations might stem from, among others, ion range uncertainties, day-to-day variations in patient positioning, or anatomical

changes in the patient during the treatment course. To verify that the patient has been treated with the intended dose distribution, an *in-vivo* method to measure the characteristics of the dose delivery is needed.

Since the particles stop at the end of their range inside the patient, secondary signals need to be used for dose verification. Most verification methods depend on the imaging of positron-emitting nuclei or prompt gamma rays, which are created via nuclear interactions between the particle beam and the patient. For an overview of these nuclear techniques, we refer to the reviews by Studenski and Xiao (2010), Parodi (2011), Fiedler *et al* (2012), Zhu and El Fakhri (2013), Knopf and Lomax (2013), Kraan (2015), and Parodi (2015). A completely different technique, currently under investigation is the detection of thermoacoustic waves generated by a local increase in temperature, due to absorbed dose using an ultrasound probe (Hayakawa *et al* 1995, Assmann *et al* 2015, Jones *et al* 2015).

Some prompt-gamma imaging prototypes are currently being tested in a clinical setting; see, e.g., Verburg and Bortfeld (2016) and Richter *et al* (2016). However, the method that so far has been tested most extensively in a clinical environment is Positron Emission Tomography (PET). In a few therapy centers, dose delivery verification using PET is in routine clinical use (Kurz *et al* 2015, Nishio *et al* 2010). The most abundant positron-emitting nuclei that are created by particle beams are ^{15}O, ^{11}C, ^{30}P, and ^{38g}K with radioactive half-lives between 2 and 20 minutes. This points to a fundamental drawback of PET, when compared to prompt-gamma imaging: instantaneous feedback is practically impossible. Also, separate verification of different irradiation fields is difficult, since counts from all fields will be mixed in the PET image, usually eliminating the sharp distal and lateral edges. Lastly, since a measurement takes between 2 and 20 minutes, the positron-emitting nuclei are transported away from the place where they were created via biological/physiological processes: the so-called biological washout of the PET nuclei (Mizuno *et al* 2003, Hirano *et al* 2013, Helmbrecht *et al* 2013, Grogg *et al* 2015). This also degrades the quality of the PET image.

Placing a PET scanner at the treatment position (*in-situ* PET) and measuring during the irradiation, either while the beam is on (beam-on PET) or in-between synchrotron spills, mitigates most of these problems. The highest number of counts is obtained in this way, implying that the measurement time can be shorter, thereby minimizing the biological washout. PET imaging in-between synchrotron spills was introduced by Enghardt *et al* (2004). A scanner based on the DoPET system is used to take PET data during beam-on (Sportelli *et al* 2016, Rosso *et al* 2016). A prototype of the PET scanner, being developed by the INSIDE project, is capable of taking data during synchrotron spills (Piliero *et al* 2016).

When a PET scanner takes data with the beam on, also very short-lived nuclides are measured. The most important short-lived nuclide for proton therapy is ^{12}N, which has a half-life of 11 ms (Dendooven *et al* 2015). For carbon-rich tissue, the production is such that ^{12}N can dominate the total counts up to 70 seconds after the start of an irradiation. The short half-life, combined with the high production, makes it possible to use *in-situ* PET to provide feedback on the dose delivery on a sub-second timescale. So far, the integrated production of ^{12}N has been measured, but it has not yet been imaged using a PET system. The purpose of this paper is to provide a proof-of-principle for the use of beam-on PET imaging of short-lived ^{12}N nuclei for proton therapy dose delivery verification.

2 Materials and methods

2.1 Irradiation setup

The experiment was performed at the AGOR cyclotron irradiation facility at KVI-Center for Advanced Radiation Technology (KVI-CART), University of Groningen. This facility operates a fixed horizontal beam line. Figure 1 shows a picture of the experimental setup. A beam of molecular H_2^+ ions was accelerated to 90 MeV per nucleon with a bunch repetition frequency of 44.4652 MHz. Directly after the exit foil at the end of the beam pipe, an air ionization chamber (the beam intensity monitor, BIM) was placed to measure the beam intensity. During its calibration, the beam intensity was lowered until the number of protons

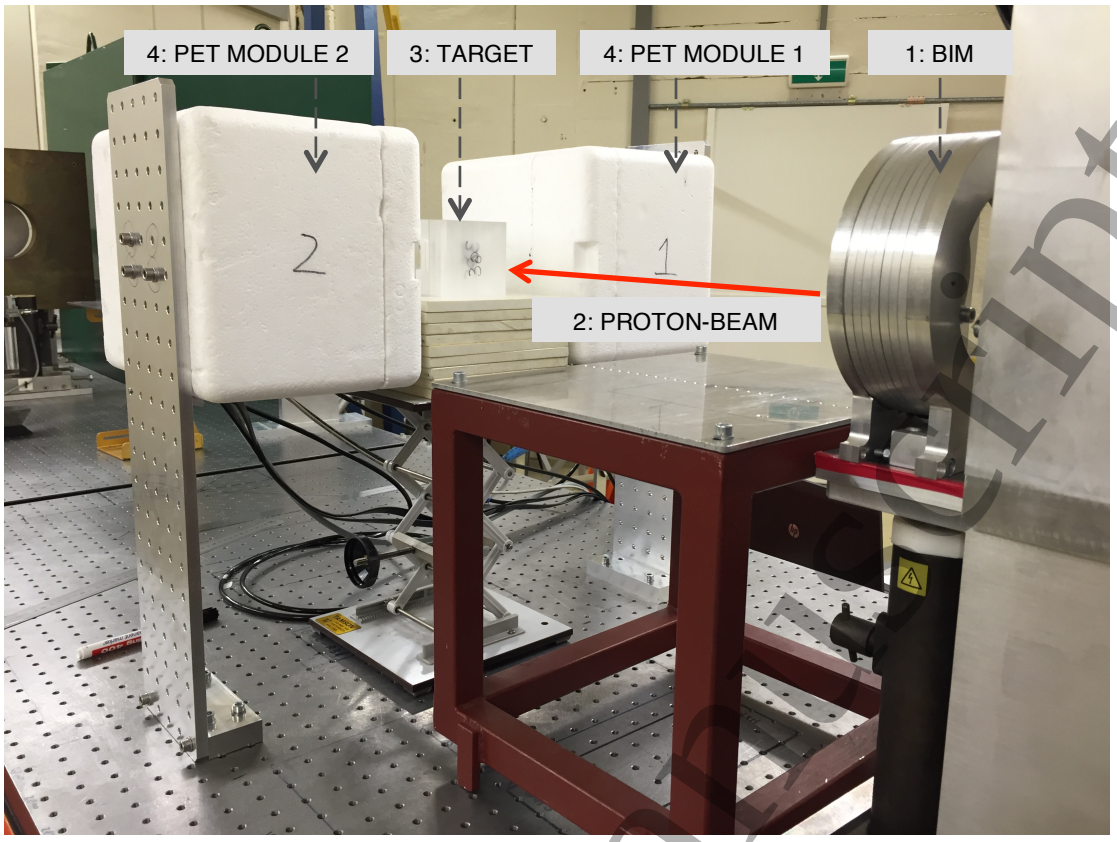

Figure 1. The Module TEK PET setup at KVI-CART. 1) Beam Ionization Monitor, used for measuring the beam intensity. 2) 90 MeV/u H_2^+ beam. 3) Target positioned on top of spacer plates. PMMA and graphite targets were used. 4) PET modules from the Module TEK system inside a Styrofoam box.

could be counted with a scintillation detector. The corresponding number of monitor units (MUs) from the ionization chamber was thus related to the number of protons.

Most measurements were done at an instantaneous beam intensity of 6.2×10^8 pps. This is about one order of magnitude lower than a typical beam intensity used in clinical facilities. A beam of 2 cm full width at the target position was used. The width and position were verified using a harp-type (wire grid) beam profile measurement system.

The proton beam was stopped in two target materials: graphite and PMMA. The graphite target was a cube of $50 \times 50 \times 50$ mm^3. The PMMA target was a block of $96 \times 96 \times 110$ mm^3, with the long side of the target placed parallel to the beam direction. The proton beam was centered on the targets. Using the PSTAR database (Berger *et al* 2005), the range of 90 MeV protons in graphite and PMMA was calculated to be 4.2 cm and 5.5 cm, respectively. The targets were placed such that the PET distribution ended just after the center of the field of view (FOV) of the detectors. Vertically, the center of the detectors, the proton beam and the center of the targets were aligned. The distance between the front faces of the detector modules was 32.8 cm.

In order to disentangle the contribution of the short-lived ^{12}N from the longer-lived nuclei in the PET image, the proton beam macro structure was pulsed on a millisecond timescale. The pulsing was controlled by an arbitrary waveform generator (Tektronix AFG 3252C), which controls the voltage on a set of fast electrostatic deflection plates in the injection line of the cyclotron. This way, the beam was either deflected away from or into the cyclotron, delivering the desired time structure.

2.2 Module TEK PET system

The Module TEK PET system from Philips Digital Photon Counting (Haemisch *et al* 2012) was used. This system uses lutetium-yttrium oxyorthosilicate (LYSO) scintillating crystals mounted on digital silicon photomultipliers (dSiPM). The Module TEK system consists of two opposing PET modules. Each module is made from a 2 × 2 array of tile sensors of 32.6 × 32.6 mm^2. Each tile consists of a matrix of 4 × 4 sensor dies, which each contain 4 pixels in a 2 × 2 configuration. The pixels are further divided into 4 sub-pixels. A LYSO crystal of 3.8 × 3.8 × 22 mm^3 is coupled to each pixel, for a total of 16 × 16 LYSO crystals in a PET module.

In order to minimize noise in the data due to thermally induced triggers, i.e. dark counts, low signal level triggers are suppressed using a trigger threshold. The system was operated in so called *trigger 4* mode, which means that all four individual sub-pixels of a pixel must see a discharge in order to generate a valid trigger. After the trigger threshold, a validation threshold is introduced, which is related to the spatial distribution of microcell discharges on a pixel (Frach *et al* 2010).

To minimize the dark count rate (DCR), the system temperature was actively maintained at 3 °C using Peltier elements, a copper heat sink, and an ethanol cooling system. The modules were placed in separate Styrofoam boxes, which were continuously flushed with dry nitrogen gas to prevent condensation. The total DCR was further reduced significantly by disabling the top 20% of the microcells that exhibited the highest DCR (Somlai-Schweiger *et al* 2015).

For our application, we need to measure the time of the PET event with respect to the cyclotron RF phase with sufficient accuracy. This creates the possibility to distinguish between events that are correlated with a proton bunch, e.g. prompt gamma rays, and events that are not correlated in time with the proton bunches, e.g. PET events. The cyclotron RF period was equal to 22.5 ns, with proton bunches of about 2 ns full width. Event timing with respect to the RF period was implemented by using the cyclotron RF signal as a clock that drives the sensor time-to-digital converters (TDC).

Data was acquired in singles mode and coincidence sorting was done off-line. The Module TEK was connected to a data acquisition laptop by a USB 2.0 interface, which has a maximum raw signaling rate of 480 Mbit/s (Compaq *et al* 2000). This is not enough to capture the full singles rate that is expected with the proton beam on, as previously noted by Cambraia Lopes *et al* (2016), causing loss of data.

The electronic time skew between TDC-times reported from different dies was corrected for in order to obtain the best possible coincidence resolving time (CRT). A procedure analogous to Cambraia Lopes *et al* (2016) was followed to obtain the time skew corrections for all 64 × 64 die-pairs between module 1 and module 2. A maximum correction of 1.62 ns was found. In *trigger 4* mode these corrections resulted in a CRT with a full-width at half-maximum (FWHM) of 0.78 ns.

2.3 Efficiency of the detector setup

The coincidence detection efficiency of the detector setup was measured by moving a calibrated ^{22}Na source of 1 mm diameter in the midplane between the detector modules. For this purpose, it was considered a point source. The source has a strength of 382 kBq. By scanning the source from the center to the outer edge of the FOV in the x- and y-direction, the efficiency at different positions was measured. The setup can be assumed symmetrical in the top-to-bottom and the left-to-right directions. The source was thus only scanned in one quarter of the midplane using a grid of 6 × 6 points spaced 6.5 mm apart. Because of symmetry, the efficiency in the entire plane was calculated and fitted using a product of linear functions

$$\text{efficiency}(x, y) = (-a|x| + b) \cdot (-c|y| + d) \qquad (1)$$

with a, b, c, and d parameters of the fit. The quality of the fit was evaluated using the coefficient of determination (R^2) adjusted for the number of degrees of freedom in the fit.

2.4 Beam-on detector performance

2.4.1 Beam-on singles count rate To characterize the performance of our in-situ beam-on PET system while the beam is on, the dependence of the count rate on beam intensity was investigated. Due to the USB 2.0 bottleneck described in section 2.2, measuring with a continuous beam saturates the data acquisition system at fairly low beam intensities. However, it is possible to take good quality beam-on data, as we will show.

A pulsed beam with a total period of 120 ms and 50% duty cycle, resulting in 60 ms beam-on, followed by 60 ms beam-off was used. The instantaneous beam intensity, meaning the beam-on intensity, was increased from 2×10^7 pps to 5×10^9 pps in several steps. A total measuring time of 120 s was used for all acquisitions. Fresh PMMA targets were installed for each measurement, eliminating any residual activity in the target.

2.4.2 Beam-on spectra To investigate the quality of the beam-on and beam-off data, energy and time spectra were taken for beams of 6.2×10^8 pps and 5.0×10^9 pps. A graphite target was installed and the beam was pulsed with a period of 89 ms and a beam-on duty cycle of 33%, meaning 30 ms beam-on followed by 59 ms beam-off. The total irradiation time was 120 s. A coincidence window of 10 ns was used. A more strict event validation setting was used during the 5.0×10^9 pps measurement, resulting in the suppression of low energy events.

2.5 Data analysis

Coincidence sorting was done off-line with an initial coincidence window of 10 ns. The energy and scintillation crystal, in which the interaction took place, was defined by the pixel with the maximum recorded energy on the triggering sensor die. Energy cuts were applied after calibrating the photon counts at 511 keV.

2.5.1 Timing calculation at different time scales Each single event is identified in time by a 16 bit frame-number, which is subdivided in 24 bit TDC bins. A frame lasts 368.5 µs and each TDC bin corresponds to 21.96 ps. The clock time since the start of the measurement was calculated using these values. Since pulsed proton beams were used, the time of the event within the beam pulse, t_{pulse}, was calculated by applying the modulus operator

$$t_{pulse} = t_{clock} \bmod T \qquad (2)$$

where t_{clock} is the clock-time, and T is the period of the pulsing cycle. The same procedure was used to calculate the time of the event with respect to the cyclotron RF signal, t_{RF}

$$t_{RF} = TDC \bmod T_{bunch} \qquad (3)$$

where TDC is the recorded TDC bin and T_{bunch} is to the number of TDC bins for one RF cycle.

2.5.2 Prompt-gamma rejection Prompt gamma events are directly correlated with the proton bunches. These prompt gamma counts are background in our PET application, so they need to be separated and removed from the PET counts. Prompt counts are detected during proton bunches, so a histogram was made of the number of counts vs. t_{RF}. The events in the prompt peak were removed from the data stream using an anti-coincidence filter.

2.5.3 ^{12}N nuclide detection ^{12}N was identified using the time t_{pulse}. During each beam-on part of a pulse, long-lived and short-lived positron-emitting nuclei are produced and the resulting PET count rate grows on top of a prompt background. When the beam is turned off, the prompt background stops and the PET detectors only detect the radioactive decay of the positron-emitting nuclei. At the time scale of the beam pulsing, the longer-lived nuclides are expected to be seen as a constant background under a clearly visible ^{12}N decay ($t_{1/2}$ = 11 ms). As the irradiation progresses, the background from the longer-lived nuclides increases.

A pulsed beam of 6.2×10^8 pps instantaneous beam intensity was used on a graphite target. The total irradiation time was 120 seconds, using a pulsing period of 89 ms. The beam

was off from 0 – 59 ms and on from 59 – 89 ms. A coincidence window of 6 ns was applied to the data, and the full energy peak was selected via an energy window of 300 – 650 keV for both detectors. The coincidences corresponding to the proton bunches are cut out of the data using the anti-coincidence filter. The remaining non-prompt PET data was then used to make the time distribution of PET counts within the pulsing cycle.

The total number of detected counts corresponding to ^{12}N nuclei was calculated by fitting the beam-off part of the time spectrum of the coincidences with a ^{12}N decay curve. The decay curve used is

$$A(t) = A_0 \exp\left(-\lambda_{N12} t_{pulse}\right) + C \quad (4)$$

with A the measured time-activity profile, A_0 the ^{12}N activity at the start of the beam-off period, λ_{N12} the known decay constant of ^{12}N, and C the constant activity on this timescale due to longer-lived nuclei. The total number N of measured ^{12}N counts is given by

$$N = \frac{A_0}{\lambda_{N12}} \quad (5)$$

2.5.4 Imaging Two-dimensional imaging was implemented by plotting a 2D histogram of the intersection points of the lines of response (LOR) with the midplane between the two detector modules. The width of the positron annihilation spatial distribution was determined by the proton beam size and the positron range. The proton beam full width was about 2 cm, with an RMS of about 4 mm. For ^{12}N with a 1D RMS range of 18 mm in water (Dendooven *et al* 2015), corresponding to 10.6 mm in graphite, the positron range was the main contribution to the width of the annihilation spatial distribution. As the width of this distribution was much smaller than the distance between the detectors, using the two-dimensional imaging method was justified.

A sensitivity correction was applied to the image by dividing the pixel value in the image with the measured efficiency at that point. The sensitivity correction factors were normalized such that the correction factor in the center of the FOV was equal to 1. More sophisticated image reconstruction techniques, such as 3D maximum-likelihood expectation-maximization (MLEM) will in general produce better images. However, for fast range verification on the level of single pencil beams, a 3D reconstruction method is not necessary.

2.5.5 Separation of short and long-lived nuclides There is no way to tell whether a coincident event stems from a short-lived or a long-lived nucleus. They both emit a positron that annihilates and emits indistinguishable 511 keV photons. The method used to separate the two contributions is based on half-life analysis. The same irradiation properties as in section 2.5.3 were used. An energy window of 300 – 650 keV and a coincidence time window of 6 ns were applied to the data. The first step was to make an image using t_{pulse} from 0 – 40 ms. This contains coincidences that are detected just after a beam pulse has ended, i.e. where the contribution from ^{12}N is highest. The second step was to make an image using t_{pulse} from 40 – 59 ms. Since the half-life of ^{12}N is 11 ms, this image starts after almost 4 half-lives of ^{12}N. Only 8% of the ^{12}N is left at the start of the second image, which means its contribution is minimal. Mostly long-lived nuclei are present in this image. The ^{12}N distribution was then calculated by subtracting the long-lived image from the first image, after applying a weighting factor w to the second image of

$$w = \frac{\Delta t_1}{\Delta t_2} = 2.11 \quad (6)$$

with Δt_1 and Δt_2 the length of the time window of the first and the second image, respectively. This factor is applied since the number of counts of the long-lived nuclides scales with the length of the time window.

2.5.6 Detection of proton range shifts Measurements were done for two positions of the target that differ by 5 mm in the beam direction. The 50% distal fall-off position x_0 was measured by fitting the distal edge of a 1D projection with a sigmoid function

$$S(x) = base + \frac{max}{1+\exp\left(\frac{x_0 - x}{rate}\right)} \quad (7)$$

The measured range shift between the two target positions is then defined as the difference between the 50% distal fall-off positions.

2.6 Simulation of ^{12}N imaging for a large scanner

A simulation study using the GATE simulation framework (Jan *et al* 2004) was performed to estimate the precision and accuracy with which a proton range shift of 5 mm can be seen using ^{12}N imaging with a large dual panel scanner. A single spot from the distal energy layer of an irradiation was simulated, containing 5×10^8 instantaneously delivered protons of 90 MeV. A separate simulation was performed for a spot of 1×10^8 protons. The imaging procedure started directly after the protons were delivered, and the scanning time was such that all ^{12}N had decayed. Assuming that the distal layer is delivered first, the number of counts from long-lived nuclides is much smaller than that from ^{12}N (Dendooven *et al* 2015); long-lived nuclides were therefore ignored in the simulation. In order to be able to compare with the experimental results, the phantom consisted of the same graphite target that was used for the experimental measurements, i.e. a $50 \times 50 \times 50$ mm^3 block with a density of 1.7 g/cm^3. Since the ^{12}N production cross-section as a function of energy is not well known, the ^{12}N distribution in the beam direction was approximated by a flat production from 90 to 48 MeV, a linear increase between 48 – 21 MeV, after which the production goes to zero, as seen in figure 2. The linear increase was based on a fit to the cross-section data from Rimmer and Fisher (1967). The transversal profile was equal to a Gaussian with a sigma of 3 mm. An overall scaling factor was applied to obtain the experimental value of ^{12}N produced by a 55 MeV proton as measured by Dendooven *et al* (2015). The positron energy distribution was implemented according to equation 9.25 from Krane (1988) and the positron stopping process was included in the simulation.

The scanner was a dual panel PET system centered on the target with a separation between the two panels of 40 cm. Each panel was comprised of a 52×52 array of LSO crystals with a size of $4 \times 4 \times 20$ mm^3. An energy resolution of 13% at 511 keV and a timing resolution of 500 ps were used. Coincidences were selected using an energy window of 400 – 650 keV and a coincidence time window of 4.5 ns. Simulations were done for two positions of the target that differ by 5 mm in the beam direction. Imaging and detection of proton range shifts were performed as described in section 2.5.4 and 2.5.6.

3 Results

3.1 Efficiency of the detector setup

The measured coincidence detection efficiency along the central axes in the midplane between the detectors is shown in figure 3. The fit, applied to all the 6×6 data points, corresponds to equation (1) with parameters $a = 0.015$, $b = 0.54$, $c = 0.015$, and $d = 0.50$, which gives the detection efficiency in percent. The adjusted coefficient of determination for this fit is $R^2 = 0.9938$, which means the fit is very good. A maximum efficiency of 0.27% is reached in the center of the FOV.

3.2 Beam-on detector performance

3.2.1 Beam-on singles count rate Figure 4 shows the singles count rate of the entire PET system, as a function of instantaneous beam intensity for the PMMA target, averaged over the 120 s irradiation (labeled "all") as well as the average singles count rates during the beam-on and beam-off periods separately. The beam-off count rate grows linearly with the beam intensity.

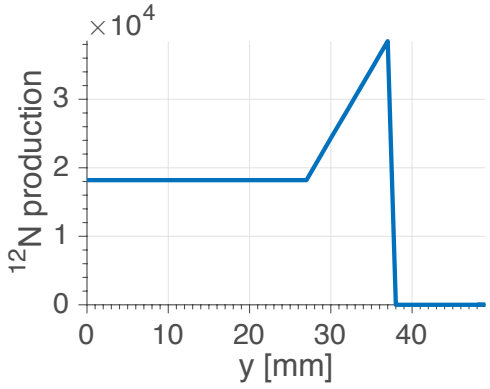

Figure 2. An approximation of the ^{12}N production in the beam direction of 5×10^8 protons of 90 MeV on a graphite target used for the GATE simulation study. The transversal direction was a Gaussian shape with a sigma of 3 mm.

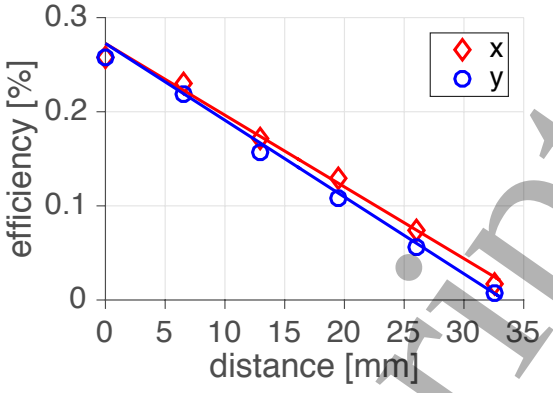

Figure 3. Coincidence detection efficiency in the midplane between the detectors along the horizontal (x) and vertical (y) axes as a function of the distance from the center of the FOV. The lines show the result of a fit applied to the data according to equation (1).

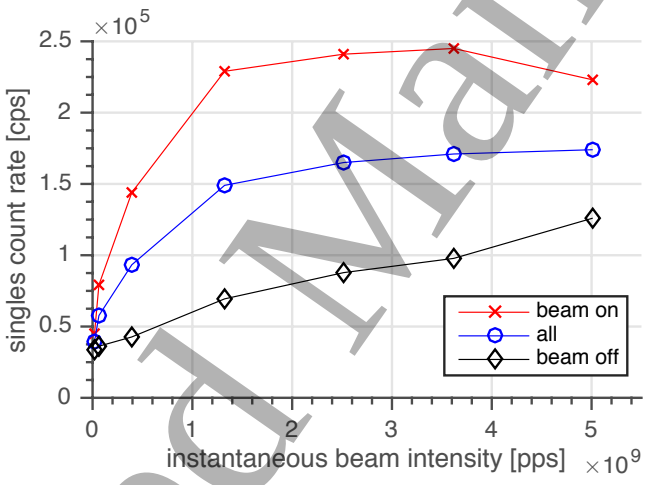

Figure 4. Singles count rate as a function of instantaneous beam intensity on a PMMA target, when using a pulsed beam of 120 ms period, 50% duty cycle, and a total irradiation time of 120 s. Shown are the count rate averaged over the 120 s irradiation ("all") as well as the average singles count rates during the beam-on and beam-off periods separately.

At a beam intensity of approximately 0.5×10^9 pps, the beam-on count rate starts to saturate, resulting in a decreasing beam-on count rate after 3.5×10^9 pps. Using a linear fit of the first two points, the slope of the beam-on count rate at low beam intensities is equal to 7.7×10^{-4} counts/incident proton. Since the saturation at low intensities is minimal, this value can be used to estimate the total singles count rate an *in-situ* PET scanner has to handle during beam-on. The total solid angle coverage of our detector setup using two heads is approximately 0.27 steradian. The expected singles count rate during beam-on for any scanner configuration is then calculated to be 2.9×10^{-3} count/(incident proton · sr). The offset of 0.30×10^5 cps at zero beam intensity is caused by the intrinsic radioactivity of the LYSO crystals. Natural lutetium contains the radioactive isotope ^{176}Lu, which decays at a rate of 200 Bq per cm^3 of

LYSO. For a crystal volume of 163 cm^3 LYSO for the entire system, the background radioactivity is thus equal to 0.33×10^5 Bq. Since these decays happen inside the scintillation crystals, practically all of them will produce a valid trigger on the sensor die and end up in the data stream.

3.2.2 Beam-on spectra The energy and time spectra are shown in figure 5. Using a linear energy calibration with only the 511 keV photopeak, the energy spectra end at 1280 keV. This represents full saturation of the dSiPM sensors, when all microcells on a pixel have discharged. The 1275 keV peak from ^{22}Na falls within this saturation region. It is possible to correct the energy calibration for this saturation effect, but since only the identification of the 511 keV photopeak is of importance for PET, no correction was applied.

Figure 5a shows spectra of all recorded coincidences of this measurement. The FWHM of the timing spectrum for the measurement at a beam intensity of 6.2×10^8 pps is equal to 1.1 ns. This timing spectrum is worse than the spectrum measured at an intensity of 5.0×10^9 pps, since the full width at tenth of maximum (FWTM) is larger. This broadening of the peak is due to the higher fraction of low energy photons in the data set. In general, lower energy photons will have a broader coincident time peak caused by the fixed level of time pickoff. These low-energy photons are suppressed in the measurement at an intensity of 5.0×10^9 pps, because a higher validation setting was used.

The full data set was then divided in beam-off and beam-on coincidences. Figure 5b shows spectra for coincidences recorded during the beam-off period (59 ms), while figure 5c shows the spectra during the beam-on period (30 ms). The FWHM of the time spectrum for the beam-off data of the measurement at an intensity of 6.2×10^8 pps is 1.0 ns, and for the beam-on data it amounts to 1.5 ns.

The beam-on data contain contributions from PET annihilations as well as prompt gamma rays, which are directly correlated in time with the protons. Applying an anti-coincidence constraint with the proton bunches removes most of the prompt counts. This procedure is shown graphically in figure 6. The prompt counts are separated and removed from the non-prompt counts. Coincidences with at least one single between t_{RF} bin number 600 and 750 are marked as prompt and removed from the data stream. Some singles outside this window are also removed, since they are part of a coincidence where the other event is inside the window. The amount of removed singles outside of the window depends on the CRT of the detectors, and the size and position of the source between the detectors. Figure 5d shows the spectra of the beam-on data with the anti-coincidence constraint applied. Most photons with energies above 511 keV are removed using this technique. A sharp 511 keV photopeak remains and the total energy spectrum looks identical to the beam-off spectrum (figure 5b). The time-spectrum of the 6.2×10^8 pps measurement is also improved to a FWHM of 1.1 ns. Figure 5e shows the data that was removed using the constraint, i.e. the counts that are in coincidence with the proton bunches. The FWHM of the time distribution of the 6.2×10^8 pps measurement is 1.6 ns.

3.3 ^{12}N nuclide detection

The coincidence counts vs. t_{pulse}, measured as explained in section 2.5.3, are shown in figure 7. When the beam turned on at t_{pulse} = 59 ms, the coincident count rate decreased from 6.2×10^2 counts per 0.89 ms bin to 2.2×10^2 counts per bin, which is a reduction of 65%. This indicates a loss of PET data by this amount during beam-on due to the data transfer limit (see section 2.2 and 3.2). A fit of the ^{12}N decay was performed from 0 – 50 ms. The total number of ^{12}N counts above the constant activity due to the longer-lived nuclides is 4.0×10^3.

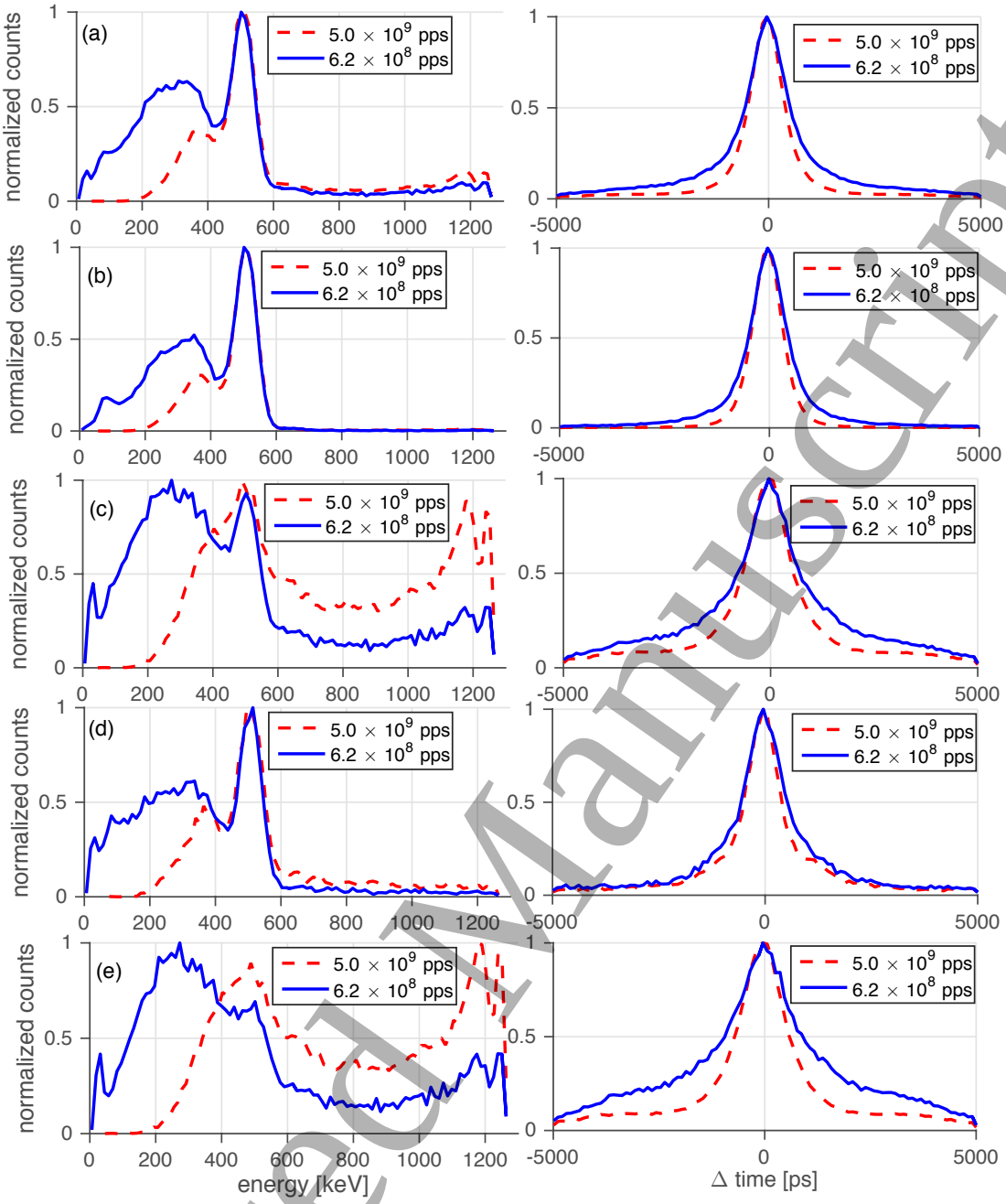

Figure 5. Energy (left) and time (right) spectra of coincidences in a pulsed irradiation using the graphite target. The spectra are normalized to their own maximum. (*a*) All data. (*b*) Data from the beam-off period (59 ms). (*c*) Data from the beam-on period (30 ms). (*d*): Coincidences from the beam-on period that *do not* coincide with a proton bunch. Prompt gamma counts are removed. (*e*) Coincidences from the beam-on period that *do* coincide with a proton pulse, mainly prompt gamma related coincidences.

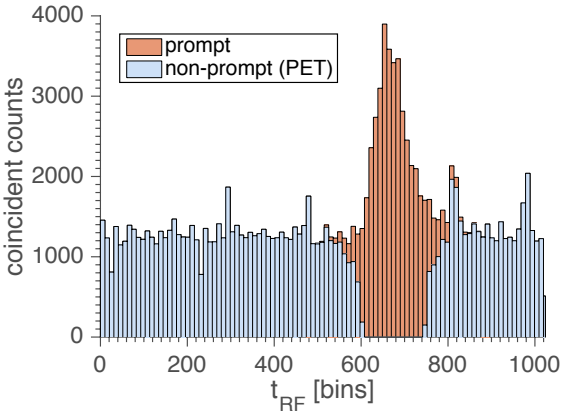

Figure 6: Distribution of coincident events over the RF cycle of 1024 TDC bins using the graphite target with a beam intensity of 6.2×10^8 pps. The t_{RF} of both singles comprising the coincident event is shown. Events coinciding with the proton bunch can be seen around bin number 700.

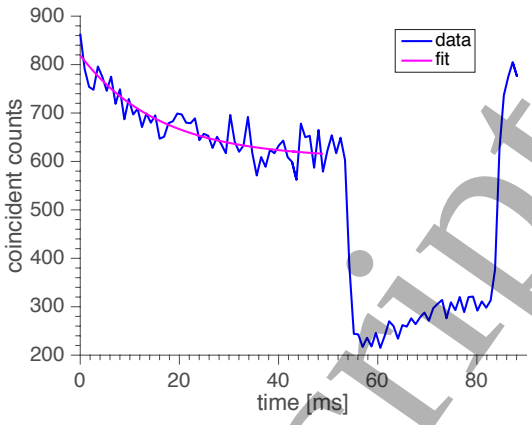

Figure 7. Distribution of coincident events as a function of t_{pulse} for a graphite target. The beam is off from 0-59 ms, and on from 59-89 ms. A fit of the ^{12}N decay during the beam-off period is shown.

3.4 Imaging, separation of short- and long-lived nuclei

The results of the 2D ^{12}N imaging procedure from section 2.5.5 are displayed in figure 8. The ^{12}N image (figure 8c) contains mostly positive pixels, which indicates a net contribution of ^{12}N counts. Negative values occur due to statistical fluctuations.

One-dimensional projection profiles on both axes are shown in figure 9. The ^{12}N profiles as seen in figure 9c are in both the x– and y–direction broader than the profiles of the longer-lived positron emitters in figure 9b. Figure 9d is a comparison of the long-lived and ^{12}N profiles for the first target position (labeled as "0 mm"). A widening of the profiles is clearly seen. The width (RMS) of the sensitivity corrected transversal profile is 8 ± 3 mm for the long-lived positron emitters and 12 ± 3 mm for ^{12}N .The quadratic difference of 9 ± 5 mm is interpreted as being due to the range of the ^{12}N positrons, which have a 1D RMS range of 10.6 mm in graphite. This is consistent with the measured increase in the width of the transversal profile. The 1D RMS positron range for ^{15}O, the nuclide that provides most of the long-lived contribution, is 0.7 mm in graphite and thus negligible with respect to both the beam width and the PET scanner spatial resolution.

A sigmoid was fitted to the distal edge of the profiles in the beam direction for the images of the long-lived positron emitters (figure 9b) and ^{12}N (figure 9c). The proton range shift of 5 mm was measured by the difference in the x_0 parameter of the fit. For the profiles of the long-lived nuclides in figure 9b, a shift of 5.6 ± 0.4 mm is measured between the two target positions, while a shift of 6 ± 3 mm is found for ^{12}N in figure 9c.

3.5 Simulation of ^{12}N imaging for a large scanner

The results of the simulations of 90 MeV protons stopped in a graphite target that is imaged by a large dual panel PET scanner (see section 2.6) are displayed in figure 10. For a spot of 5×10^8 protons, the total number of detected coincident counts is equal to 1.2×10^4. The whole positron emitter distribution falls within the FOV of the detector, so the loss of counts at the entrance of the target (around y = -30 mm) due to positron escape is visible as a steeper decrease compared to the distal edge of the ^{12}N profile (at y = 14 mm). The shift of the target by 5 mm was measured by the x_0 parameter of the sigmoid (equation 7) that was fitted to the distal edge. A shift of 5.2 ± 0.5 mm is found. When the same procedure was applied for a spot of 1×10^8 protons, a shift of 5.5 ± 1.1 mm is found.

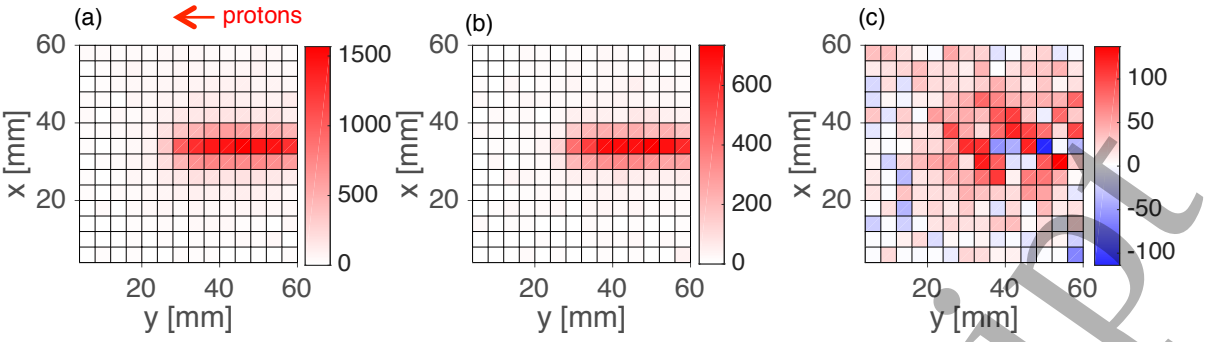

Figure 8: 2D images of the coincident counts for the first target position of the graphite target. The beam enters from the right in the –y direction. A PET detection sensitivity correction was applied. (*a*) The image is made using t_{pulse} from 0 – 40 ms, including both ^{12}N and long-lived nuclei. (*b*) The image is made using t_{pulse} from 40 – 59 ms, including mostly long-lived nuclei. (*c*) The ^{12}N image is obtained by subtracting the weighted long-lived image from the first image.

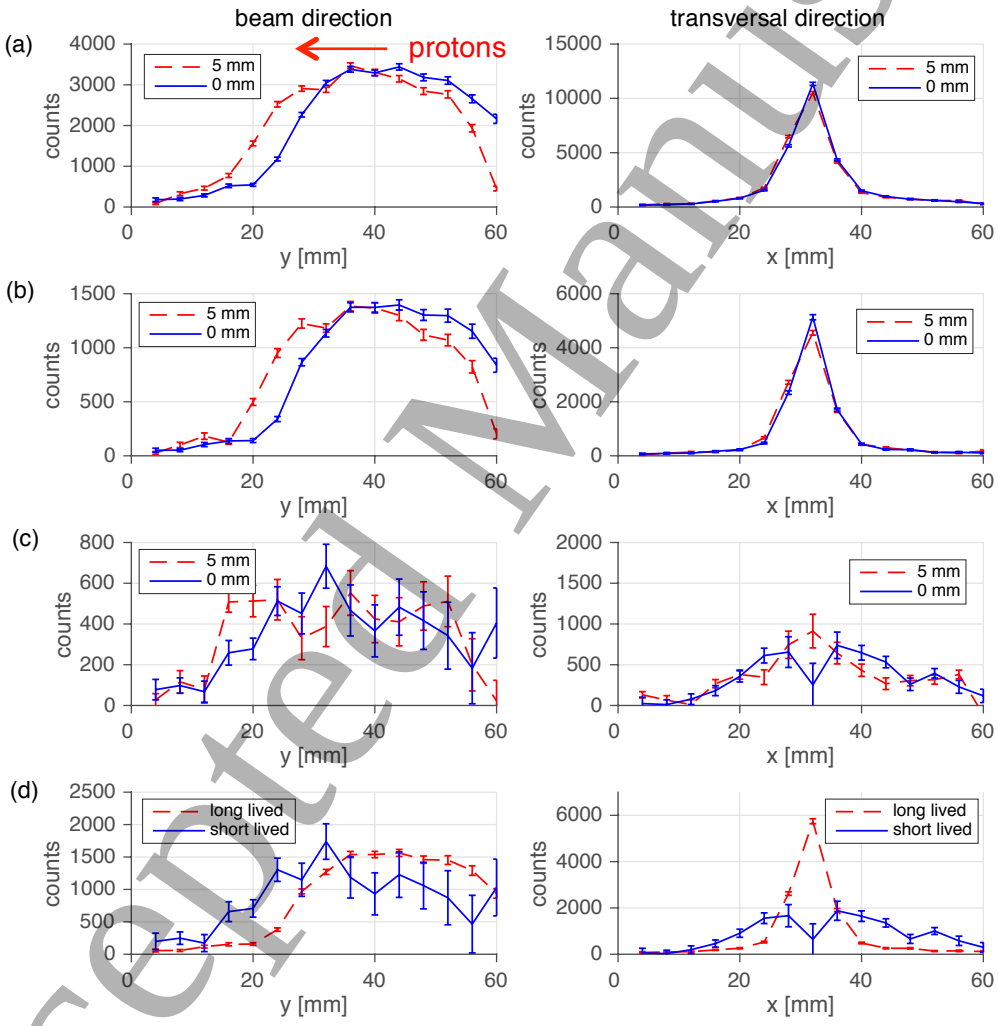

Figure 9: 1D projection profiles of the 2D images of figure 8 for the first target position (labeled as "0 mm") and for the target shifted by 5 mm. The beam enters from the right in the -y-direction. The x-direction is transversal to the beam. The profiles are normalized to an equal number of total counts. (*a*) t_{pulse} from 0 – 40 ms. (*b*)*:* t_{pulse} from 40 – 59 ms. (*c*) ^{12}N profile. (*d*) Comparison of the long lived and ^{12}N profile for the "0 mm" target position.

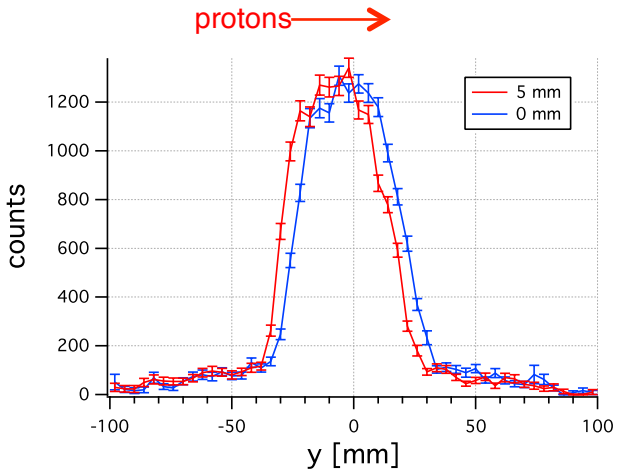

Figure 10: 1D ^{12}N profiles from simulations of 90 MeV protons stopped in a graphite target that is imaged by a large dual panel PET scanner. The instantaneous delivery of 5×10^8 protons in a single beam spot is assumed. Profiles for two target positions shifted by 5 mm in the -y-direction are shown.

4 Discussion

4.1 Beam-on detector performance

From the singles count rates, figure 4, it can be seen that the count rate of the Module TEK suffers from saturation above a beam intensity of approximately 0.5×10^9 pps. Not all events are transmitted by the data acquisition system. The beam-on singles count rate even decreases for intensities beyond 3.5×10^9 pps. However, the beam-on data that is transmitted is of good quality; see figure 5. Once the prompt events that coincide with the proton bunches are removed from the data via an anti-coincidence filter, high-quality PET energy and time distributions result. This shows that it is possible to take good PET data during beam-on by removing prompt counts using the anti-coincidence filter.

Helmbrecht *et al* (2016) point out that for typical PET block detectors, it is challenging to perform prompt-gamma-ray-free imaging, due to pile-up of positron annihilation photons and prompt gamma rays. They used a PET detector with LSO crystals and a cyclotron with a proton bunch repetition period of 9.4 ns and a proton energy dependent bunch duration of 0.2 – 2 ns. LSO has a characteristic decay time of 40 ns. So if a prompt gamma ray is detected, it is not possible to detect a 511 keV photon using the same detector without pile-up before the next proton bunch. Whether a detector can be used for beam-on PET then depends on this pile-up probability, which in turn depends on the count rate and thus detector surface area. Helmbrecht *et al* use a Siemens PET block detector of 52×52 mm^2 at 18.5 cm from the beam. The count rate measurements that we have presented show a count rate of about 55 kcps per cm^2 detector area at 18.5 cm distance from a 1 nA beam. For the block detector, this means a count rate of about 1.5 Mcps. In this case, a beam-on 511 keV PET count will often be summed with a prompt gamma count. Helmbrecht *et al* mitigate this problem by a pile-up rejection technique that removes these events. The PDPC Module TEK PET system we used is based on dSiPMs that are read out at the level of a die. This basic detector unit has a surface area of about 0.6 cm^2, greatly reducing the pile-up with prompt gamma rays. The measurement at a near-clinical instantaneous beam intensity of 5.0×10^9 pps shows that it is possible to use the anti-coincidence filter to obtain good 511 keV identification and prompt-gamma rejection.

For shorter proton bunch periods, the prompt gamma ray time window represents a larger fraction of a period and consequently a smaller fraction of PET events will pass through the anti-coincidence filter. Higher energy protons, due to a slowing down time in the order of nanoseconds, exhibit a broadening of the prompt gamma time peak, again reducing the fraction of PET events that pass through the anti-coincidence filter. For example, the Ion

Beam Applications (IBA) C230 fixed-energy cyclotron, which is widely used in proton therapy, has a bunch repetition period of 9.4 ns and a bunch duration of 0.2 ns FWHM at its maximum energy of 230 MeV up to 2 ns at 70 MeV (Petzold *et al* 2016). The longer slowing down time of higher-energy protons is in a sense compensated by the shorter bunch duration. To investigate the influence of these two properties on the anti-coincidence filter, an average value of 150 MeV with a bunch duration of 1 ns is used. The slowing down time of 150 MeV protons in a PMMA target is approximately 1.3 ns according to figure 2 of Golnik *et al* (2014). These effects need to be combined with the PET time resolution of approximately 0.5 ns FWHM. The time resolution can be quadratically summed with the bunch duration, which leads to a bunch duration of 1.1 ns FWHM. This can be convolved with the slowing down time of 1.3 ns, leading to a prompt gamma pulse with a full width of approximately 2.4 ns. If the anti-coincidence window is increased by 0.5 FWHM on each side to capture the full prompt gamma peak, 3.5 ns are discarded out of a total period of 9.4 ns. This would lead to a decrease in the accepted PET count rate during beam-on of 37%. So when using the clinical beam structure of the IBA C230 cyclotron, it would still be possible to use the anti-coincidence filter to remove prompt counts from the beam-on data.

4.2 Imaging

To obtain an image of only the ^{12}N nuclides, a method was developed to subtract the long-lived background from the image including ^{12}N. A quadratic increase of 9 ± 5 mm in the transversal size of the ^{12}N PET profile was measured, which is consistent with the ^{12}N positron range in graphite of 10.6 mm RMS. The same effect plays a role in the beam direction as well, causing a broadening of the distal edge. However, a broadening of the distal edge can also be due to a different energy dependence of the ^{12}N production cross section compared to production cross sections of the long-lived nuclides.

Dendooven *et al* (2015) show that the PET signal during the delivery of the distal layer of a patient irradiation (in case it is delivered first) will be largely dominated by ^{12}N. In our measurements, the low detection efficiency of the PET system was in a sense compensated by a long measurement time of 120 s. Due to this long measurement time, the number of counts from long-lived nuclides was much larger than it would be in a clinical irradiation of a distal layer. The resulting large correction for long-lived nuclides contributes to the uncertainty in the ^{12}N profiles. A simulation was performed to estimate the improved uncertainty in a clinical irradiation of a distal layer. When simulating a large dual panel scanner that focuses on the distal edge of the ^{12}N production, 1.2×10^4 coincident counts are detected for a spot of 5×10^8 protons. This is a few times more than in the measurements presented where we obtained ^{12}N 1D profiles containing about 4.0×10^3 counts (see section 3.3). The simulation demonstrate that a large dual panel scanner, imaging a single spot from a clinical irradiation directly after it is delivered, can measure a 5 mm range shift with millimeter accuracy: 5.5 ± 1.1 mm for 1×10^8 protons and 5.2 ± 0.5 mm for 5×10^8 protons. Due to the absence of a long-lived contribution and the higher number of counts, this is substantially better than the shift of 6 ± 3 mm deduced from the experiments presented in this work. The accuracy of this method can be compared to that of the knife-edge slit prompt gamma camera, which is the prompt gamma ray imaging device closest to clinical implementation. Figure 17 of Perali *et al* (2014) shows that approximately 1×10^9 protons of 100 MeV are needed to obtain a precision of 0.5 mm (1σ), and 2×10^8 protons are needed for a precision of 1 mm (1σ). The ^{12}N imaging technique can thus reach the same precision with half the number of protons, or a better precision can be reached with ^{12}N imaging using the same number of protons.

4.3 Clinical implementation and cost

During a patient irradiation, one could separate ^{12}N from the long-lived nuclides by for instance introducing an artificial beam-off period of 100 ms every second, or by extending the spot-switching time between different spots in a pencil beam scanning irradiation, or by using the PET data measured in-between synchrotron spills or in-between energy layers. This way, contributions from previous irradiation fields are also removed, thus providing ^{12}N PET images free from contamination from earlier fields. Integration over (part of) the distal edge

can be used to obtain better statistical accuracy, with the drawback of averaging the proton range measurement over a larger area.

Using ^{12}N imaging, accurate feedback on the dose delivery can be obtained within seconds after the start of the treatment. This technique can thus be used for on-line adaptive treatment or as an immediate indicator for off-line replanning, just as any dose delivery verification technique based on prompt gamma rays. All these techniques can potentially stop an irradiation in (near) real time when a deviation from the intended dose delivery is measured. In a more sophisticated implementation, one can envision an automatic feedback to the beam delivery system to e.g. slightly adjust the beam energy to the measured proton range. An interesting option is to use a carefully selected set of "pilot" spots from the distal layer for which the time structure is optimized for ^{12}N imaging, by e.g. allowing a sufficiently long time between these spots. If no deviations are detected using these pilot spots, one can have some confidence that the full irradiation will be delivered as intended. If deviations are detected, the treatment plan might, depending on the nature of the deviations, be recalculated on-line after which the irradiation can be completed. For example, an overall range deviation due to an error in the translation of planning CT to proton stopping power could be instantly corrected. The same *in-situ* PET system can also be used to acquire a separate image after the dose has been delivered, as PET is nowadays in use in a few therapy facilities. Such an image will be of better quality that the ^{12}N image due to the improved spatial resolution and statistics, and can be used for off-line adaptive treatment.

Cost is an important aspect of the implementation of in-vivo dose delivery verification. In the following, we investigate a number of relevant factors in the comparison of an *in-situ* dual panel PET system with the prototype of the knife-edge slit prompt gamma camera (Perali *et al* 2014). Both systems are based on comparable scintillation detectors: 2 to 3 cm thick LSO/LYSO scintillators read out by a suitable photosensor (photomultiplier tubes or SiPMs). As the PET scanner has a larger surface area, the material cost of the PET system is expected to be higher. For the PET scanner described in section 2.6, the total LSO scintillator volume is 1.7 dm^3. The prompt gamma camera contains 0.5 dm^3 of LYSO, but a thick tungsten collimator is needed, partially offsetting the lower detector cost. We show in this paper that modern PET technology is suitable for proton therapy, even for beam-on imaging. Regular off-the-shelf PET modules can thus be used to construct an *in-situ* scanner. This application will directly profit from the technological advancements in PET imaging used for nuclear medicine. Concerning integration in the irradiation environment, we see no substantial difference between a dual panel PET scanner and a prompt gamma imaging device.

5 Conclusion

We have provided a proof-of-principle for the PET imaging of ^{12}N as a tool for proton therapy dose delivery verification. Using a PET system with a small detector unit surface area, pile-up between 511 keV annihilation photons and prompt gamma rays is limited and it is possible to reject events coinciding with proton bunches for prompt-gamma-ray-free PET imaging. A method was developed to subtract the long-lived background from the ^{12}N image by introducing a beam-off period into the cyclotron beam structure. Since the ^{12}N image disappears with a half-life of 11 ms, an estimate of the long-lived image can be obtained 40 ms after the beam is turned off. This background image can then be subtracted from the ^{12}N image. A range shift of 5 mm was measured as 6 ± 3 mm using the ^{12}N profile. A larger, more efficient, PET system with a higher data throughput capability will allow beam-on ^{12}N PET imaging of single spots in the distal layer of an irradiation with an increased signal-to-background ratio of the ^{12}N image and thus better accuracy. A simulation shows that a large dual panel scanner that images a single spot directly after it is delivered, can measure a 5 mm range shift with millimeter accuracy: 5.5 ± 1.1 mm for 1×10^8 protons and 5.2 ± 0.5 mm for 5×10^8 protons. This makes fast and accurate feedback on the dose delivery during treatment possible.

6 References

Agostinelli *et al* 2003 GEANT4 – A simulation toolkit *Nucl. Instrum. Meth. A* **506** 250–303

Assmann W, Kellnberger S, Reinhardt S, Lehrack S, Edlich A, Thirolf P G, Moser M, Dollinger G, Omar M, Ntziachristos V and Parodi K 2015 Ionoacoustic characterization of the proton Bragg peak with submillimeter accuracy *Med. Phys.* **42** 567-74

Berger M, Courset J, Zucker M and Chang J 2005 ESTAR, PSTAR, and ASTAR: stopping-power and range tables for electrons protons, and helium ions *NIST* www.nist.gov/pml/data/star/index.cfm

Cambraia Lopes P, Bauer J, Salomon A, Rinaldi I, Tabaccini V, Tessonnier T, Crespo P, Parodi K and Schaart D R 2016 First *in situ* TOF-PET study using digital photon counters for proton range verification *Phys. Med. Biol.* **61** 6203–30

Compaq, Hewlett-Packard, Intel, Lucent, Microsoft, NEC, and Philips 2000 Universal Serial Bus Specification Revision 2.0, April 27, 2000, retrieved from http://www.usb.org/developers/docs/usb20_docs/

Crespo P, Shakirin G and Enghardt W 2006 On the detector arrangement for in-beam PET for hadron therapy monitoring *Phys. Med. Biol.* **51** 2143-63

Dendooven P, Buitenhuis H J T, Diblen F, Heeres P N, Biegun A K, Fiedler F, Van Goethem M-J, Van der Graaf E R and S Brandenburg 2015 Short-lived positron emitters in beam-on PET imaging during proton therapy *Phys. Med. Biol.* **60** 8923–47

Enghardt W, Crespo P, Fiedler F, Hinz R, Parodi K, Pawelke J, and Pönisch F 2004 Charged hadron tumour therapy monitoring by means of PET *Nucl. Instrum. Meth. Phys. Res. A* **525** 284-288

Fiedler F, Kunath D, Priegnitz M and Enghardt W 2012 Online irradiation control by means of PET *Ion Beam Therapy* ed U Linz (Berlin: Springer) p 527

Frach T, Prescher G, Degenhardt C and Zwaans B 2010 The Digital Silicon Photomultiplier – System Architecture and Performance Evaluation *IEEE NSS-MIC conference record* DOI: 10.1109/NSSMIC.2010.5874069

Golnik C, Hueso-González F, Müller A, Dendooven P, Enghardt W, Fiedler F, Kormoll T, Roemer K, Petzoldt J, Wagner A and Pausch G 2014 Range assessment in particle therapy based on prompt γ-ray timing measurements *Phys. Med. Biol.* **59** 5399-422

Grogg K, Alpert N M, Zhu X, Hee Min C, Testa M, Winey B, Normandin M D, Shih H A, Paganetti H, Bortfeld T and El Fakhri G 2015 *IJROBP* **92** 453-9

Haemisch Y, Frach T, Degenhardt C and Thon A 2012 Fully Digital Arrays of Silicon Photomultipliers (dSiPM) – a Scalable Alternative to Vacuum Photomultiplier Tubes (PMT) *Physics Procedia* **37** 1546–60

Hayakawa Y, Tada J, Arai N, Hosono K, Sato M, Wagai T, Tsuji H and Tsujii H 1995 Acoustic pulse generated in a patient during treatment by pulsed proton radiation beam *Radiat. Oncol. Invest.* **3** 42–5

Helmbrecht S, Enghardt W, Parodi K, Didinger B, Debus J, Kunath D, Priefnitz M and Fiedler F 2013 Analysis of metabolic washout of positron emitters produced during carbon ion head and neck radiotherapy *Med. Phys.* **40**(9)

Helmbrecht S, Enghardt W, Fiedler F, Iltsche M, Pausch G, Tintori C and Kormoll T 2016 In-beam PET at clinical proton beams with pile-up rejection *Zeitschrift für Medizinische Physik* (in press) doi:10.1016/j.zemedi.2016.07.003

Hirano Y, Kinouchi S, Ikoma Y, Yoshida E, Hidekazu W, Ito H and Yamaha T 2013 Compartmental analysis of washout effect in rat brain: in-beam OpenPET measurement using a 11C beam *Phys. Med. Bio.* **58** 8281-94

Jan S *et al* 2004 GATE: a simulation toolkit for PET and SPECT. *Phys. Med. Biol.* **49** 4543-4561

Jones K C, Vander Stappen F, Bawiec C R, Janssens G, Lewin P A, Prieels D, Solberg T D, Sehgal C M and Avery S 2015 Experimental observation of acoustic emissions generated by a pulsed proton beam from a hospital-based clinical cyclotron *Medical Physics* **42** 7090-7097

Knopf A-C and Lomax A 2013 In vivo proton range verification: a review *Phys. Med. Biol.* **58** R131–60

Kraan A C 2015 Range verification methods in particle therapy: underlying physics and Monte Carlo modeling *Front. Oncol.* **5** 150

Krane K S 1988 *Introductory Nuclear Physics* (New York: Wiley)

Kurz C, Bauer J, Conti M, Guérin L, Eriksson L and Parodi K 2015 Investigating the limits of PET/CT imaging at very low true count rates and high random fractions in ion-beam therapy monitoring *Med. Phys.* **42** 3979

Levin C S and Hoffman E J 1999 Calculation of positron range and its effect on the fundamental limit of positron emission tomography system spatial resolution *Phys. Med. Biol.* **44** 781–99

Mizuno H, Tomitani T, Kanazawa M, Kitagawa A, Pawelke J, Iseki Y, Urakabe E, Suda M, Kawano A, Iritani R, Matsushita S, Inaniwa T, Nishio T, Furukawa S, Ando K, Nakamura Y K, Kanai T and Ishii K 2003 Washout measurements of radioisotope implanted by radioactive beams in the rabbit *Phys. Med. Biol.* **48** 2269

Nishio T, Miyatake A, Ogino T, Nakagawa K, Saijo N and Esumi H 2010 The Development and Clinical Use of a Beam ON-LINE PET System Mounted on a Rotating Gantry Port in Proton Therapy *IJROBP* **76** 277-86

Parodi K 2011 *In vivo* dose verification *Proton Therapy Physics (Series in Medical Physics and Biomedical Engineering)* ed H Paganetti (Boca Raton, FL: CRC Press) p 489

Parodi K 2015 Vision 20/20 Positron emission tomography in radiation therapy planning, delivery, and monitoring *Med. Phys.* **42** 7153

Perali I, Celani A, Bombelli L, Fiorini C, Camera F, Clementel E, Henrotin S, Janssens G, Prieels D, Roellinghoff F, Smeets J, Stichelbaut F and Vander Stappen F 2014 Prompt gamma imaging of proton pencil beams at clinical dose rate *Phys. Med. Biol.* **59** 5849-71

Petzoldt J, Roemer K E, Enghardt W, Fiedler F, Golnik C, Hueso-González F, Helmbrecht S, Kormoll T, Rohling H, Smeets J, Werner T and Pausch G 2016 Characterization of the microbunch time structure of proton pencil beams at a clinical treatment facility *Phys. Med. Biol.* **61** 2432-56

Piliero M A, Pennazio F, Bisogni M G, Camarlinghi N, Cerello P G, Del Guerra A, Ferrero V, Fiorina E, Giraudo G, Morrocchi M, Peroni C, Pirrone G, Sportelli G and Wheadon R 2016 Full-beam performances of a PET detector with synchrotron therapeutic beams *Phys. Med. Biol.* **61** N650–N666

Richter C *et al* 2016 First clinical application of a prompt gamma based *in vivo* proton range verification system *Radiotherapy and Oncology* **118** 232-7

Rimmer E M and Fisher P S 1967 Resonances in the (p,n) reaction on ^{12}C *Nuclear Physics* **A108** 561-566

Rosso V *et al* 2016 In-treatment tests for the monitoring of proton and carbon-ion therapy with a large area PET system at CNAO *Nucl. Instr. Meth. in Phys. Research A* **824** 228-32

Somlai-Schweiger I, Schneider F R and Ziegler S I 2015 Performance analysis of digital silicon photomultipliers for PET *JINST* **10** p05005

Sportelli G *et al* 2016 In-beam PET data characterization with the large area DoPET prototype *J. Inst.* **11** C02089

Studenski M T and Xiao Y 2010 Proton therapy dosimetry using positron emission tomography *World J. Radiol.* **2** 135–42

Verburg J and Bortfeld T 2016 TU-FG-BRB-06: A Prompt Gamma-Ray Spectroscopy System for Clinical Studies of in Vivo Proton Range Verification *Med. Phys.* **43** 3757

Zhu X and El Fakhri G 2013 Proton therapy verification with PET imaging *Theranostics* **3** 731–40